Multistage spin correlations in the $s = \frac{1}{2}$ stuffed hyper-star lattice $Li_2Cu_2(MoO_4)_3$

J. Khatua,[1] Taeyun Kim,[1] G. Senthil Murugan,[2,3,*] S. M. Kumawat,[4] C.-L. Huang,[4] Yugo Oshima,[5] Hiroyuki Nojiri,[6] Gerald Morris,[7] Sarah R. Dunsiger,[7] Heung-Sik Kim,[8] K. Sritharan,[2] Shankar Mani,[2] R. Sankar,[2,†] and Kwang-Yong Choi[1,‡]

[1]*Department of Physics, Sungkyunkwan University, Suwon 16419, Republic of Korea*
[2]*Institute of Physics, Academia Sinica, Taipei 11529, Taiwan*
[3]*Department of Physics, St. Joseph's College of Engineering, OMR, Chennai 600 119, India*
[4]*Department of Physics and Center for Quantum Frontiers of Research and Technology (QFort), National Cheng Kung University, Tainan 70101, Taiwan*
[5]*RIKEN Pioneering Research Institute, Wako, Saitama 351-0198, Japan*
[6]*Institute for Materials Research, Tohoku University, Sendai 980-8577, Japan*
[7]*Centre for Molecular and Materials Science, TRIUMF, Vancouver, British Columbia V6T 2A3, Canada*
[8]*Department of Energy Technology, Korea Institute of Energy Technology, Naju-si 58217, Republic of Korea*

(Received 6 November 2025; revised 12 January 2026; accepted 26 February 2026; published 24 March 2026)

The star lattice, which can be visualized as a honeycomb network with each vertex replaced by a triangle, provides a rare platform for realizing exotic quantum states such as quantum spin liquids and disorder-driven random-singlet (RS) states. Herein, we investigate the ground-state properties of the three-dimensional (3D) stuffed hyper-star lattice $Li_2Cu_2(MoO_4)_3$, which exhibits a crossover from short-range spin correlations to a disorder-driven RS-like state below $T^* \sim 15.8$ K. Thermodynamic and microscopic measurements capture this crossover through a change in the power-law behavior of various observables, from $\sim T^{0.25}$ for $T > T^*$ to $\sim T^{-0.50}$ for $T < T^*$. Upon further cooling, a quasifrozen state emerges near $T_f = 0.32$ K, likely associated with weakly coupled spin chains within the hyper-star spin network. Our results underscore the crucial role of orphan spins and weak residual interactions in stabilizing a disorder-driven quantum-disordered state in three dimensions.

DOI: 10.1103/nv1l-dgv9

I. INTRODUCTION

Quantum spin systems provide an ideal platform for exploring exotic many-body quantum phenomena driven by strong quantum fluctuations that go beyond the conventional Landau paradigm of symmetry-breaking states [1,2]. One prominent example of a quantum spin-disorder ground state is the random-singlet (RS) state. Initially established in one-dimensional (1D) spin chains, the RS state emerges when quenched exchange randomness drives the system toward a disorder-dominated fixed point [3,4]. In this regime, spins pair into singlets over a broad distribution of energy scales, forming a hierarchy of correlated singlets without breaking any global symmetry [3]. Experimentally, this manifests as a universal power-law scaling in thermodynamic quantities, predicted by renormalization group theory for infinitely disordered systems [5,6].

In recent years, the search for RS states in higher-dimensional frustrated systems has gained renewed interest, particularly in the presence of quenched disorder arising from bond randomness or site dilution [7,8]. For instance, several two-dimensional (2D) disorder-induced RS states have been reported, including the square-lattice compound $Sr_2CuTe_{1-x}W_xO_6$ [9,10] and the triangular-lattice system Y_2CuTiO_6 [11]. Similar to their 1D counterparts, these 2D RS analogs are characterized by a power-law low-energy density of states, $D(E) \propto E^{-\alpha}$, which gives rise to power-law dependencies in physical observables [12–14]. However, the realization of RS phenomenology in three-dimensional (3D) systems remains scarce. Theoretical studies suggest that in three dimensions, lattice vacancies not only lead to bond randomness but also generate emergent quasispins, localized magnetic moments associated with vacancy sites that coexist with the intrinsic bulk spins [15]. Upon increasing vacancy concentration, the density of these quasispins grows and ultimately drives the system into a quantum disorder state [15].

The RS state exists in subtle competition with the quantum spin liquid (QSL) state. While a QSL is characterized by long-range quantum entanglement and fractionalized, deconfined excitations (e.g., spinons) [16–19], the higher-dimensional RS state comprises a random network of short-range entangled singlets and emergent quasispins. Because both states lack conventional long-range order and can give rise to similar experimental signatures, distinguishing between them remains a central challenge in modern condensed matter physics [20]. Systematic investigations of frustrated magnets in the presence of quenched disorder or site dilution are therefore crucial for elucidating the distinct physical behaviors of these two quantum-disordered states.

*Contact author: nanosen@gmail.com
†Contact author: sankarndf@gmail.com
‡Contact author: choisky99@skku.edu

In this context, the star lattice, derived from a honeycomb lattice with each vertex replaced by a triangle, has emerged as a promising platform for frustration-driven quantum disorder states [21]. Unlike the bipartite honeycomb lattice, the star lattice is nonbipartite with coordination number $z = 3$, holding potential for hosting richer ground states than kagome systems [22]. While theoretical studies predict a variety of quantum phases on the pristine star lattice [23–26], the introduction of bond randomness or vacancies is expected to promote RS phenomenology manifested by a power-law magnetic susceptibility, $\chi(T) \sim T^{\alpha'(T)-1}$, with $\alpha'(T) \to 0$ as $T \to 0$ [13].

Motivated by this interplay between disorder and critical spin correlations, we investigate the ground-state properties and spin dynamics of $Li_2Cu_2(MoO_4)_3$, a stuffed 3D hyper-star lattice compound. Thermodynamic and local-probe resonance measurements establish $Li_2Cu_2(MoO_4)_3$ as a rare 3D frustrated magnet where Li-Cu site mixing induces a multistage development of spin correlations. At the higher-temperature regime, dominated by 3D random antiferromagnetic correlations, exhibits a broad heat-capacity maximum and power-law ($\sim T^{0.25}$) behavior in both the muon spin relaxation rate and electron spin resonance (ESR) linewidth down to $T^* \approx 15.8$ K. Below T^*, emergent quasispins produce low-temperature power laws ($\sim T^{-0.50}$) in magnetic susceptibility, magnetic specific heat divided by temperature, and zero-field muon spin relaxation, indicative of the formation of an RS-like state. Eventually, a quasifrozen state emerges below $T_f = 0.32$ K, likely linked to weakly coupled spin chains at the centers of the 3D hyper-star-lattice polygons.

II. EXPERIMENTAL DETAILS

Polycrystalline samples of $Li_2Cu_2(MoO_4)_3$ (LCMO) were synthesized by a standard solid-state reaction route. High-purity precursor powders of Li_2CO_3, CuO, and MoO_3 (with purity of 99.95%) were weighed in stoichiometric proportions, thoroughly mixed, and finely ground using an agate mortar to ensure homogeneity. Prior to weighing, all reagents were preheated in air at 100 °C for 24 h to remove residual moisture. The homogenized mixture was initially calcined in air at 450 °C for 48 h in a ceramic crucible. To obtain a single-phase compound, the calcined powder was subjected to successive sintering steps at 500 °C and 550 °C for 48 h each, with intermediate grindings to enhance phase purity. To confirm the phase purity and crystal structure, synchrotron x-ray diffraction (XRD) measurements were performed at the 09A beamline of NSRRC, Taiwan, at 120 K. The diffraction patterns were analyzed using the Rietveld refinement with the GSAS software package [27].

Magnetic measurements, including dc magnetic susceptibility and isothermal magnetization, were carried out using a superconducting quantum interference device vibrating-sample magnetometer (SQUID VSM, Quantum Design, USA) in the temperature range of 2–300 K under magnetic fields up to 9 T. In addition, ac magnetic susceptibilities were measured by the SQUID VSM in the temperature range of 2–10 K at low frequencies ($\leqslant$950 Hz). For measurements in the lower-temperature range of 0.05–4 K, ac magnetic susceptibility was measured using a physical property measurement system (PPMS, Quantum Design, USA) equipped with a dilution refrigerator insert.

Pulsed-field magnetization measurements at 0.5 K were performed at the Institute for Materials Research, Japan, using pulsed magnetic fields with the induction method employing a pickup coil device and a ^{3}He cryostat. Specific-heat measurements were recorded using a standard relaxation method in a PPMS in the temperature range 0.2 K $\leqslant T \leqslant$ 300 K in several magnetic fields up to 9 T.

ESR experiments were conducted at RIKEN using a conventional X-band spectrometer (JEOL, JES-RE3X; $f =$ 9.12 GHz). A continuous-flow ^{4}He cryostat was employed to maintain precise temperature control in the range of 3.8–60 K.

Muon spin relaxation (μSR) measurements were conducted at the M20 beamline of TRIUMF (Vancouver, Canada) under zero-field (ZF), longitudinal-field (LF), and weak-transverse-field (wTF) conditions. About 0.5 g of powder samples was enclosed in a 2.5 μm Mylar envelope (sample area $\sim$1.3 × 1.3 cm^2) and further wrapped in 50 μm Scotch aluminum tape to minimize background signals from the copper holder. The assembly was fixed onto a copper fork sample stick and cooled using a ^{4}He flow cryostat, providing stable temperature control between 2 and 120 K. The time evolution of the muon spin asymmetry was analyzed using the MUSRFIT software package [28].

Density functional theory (DFT) calculations were performed using the OPENMX code within the generalized gradient approximation of Perdew-Burke-Ernzerhof (GGA-PBE) exchange-correlation functional [29], incorporating an on-site Hubbard $U = 6$ eV to account for Cu $3d$ correlations. The self-consistent results were subsequently used in the J_X code to evaluate the exchange coupling parameters J_{ij}^{GGA} through the Green's function based Liechtenstein approach [30].

III. RESULTS

A. Rietveld refinement and crystal structure

To confirm the phase purity and crystal structure of the polycrystalline samples of LCMO, Rietveld refinement of the synchrotron XRD data was performed using the GSAS software [27]. Figure 1(a) presents the refinement profile, which confirms the absence of any detectable secondary phase. The initial atomic coordinates for the refinement were taken from the previous structural report [31,32], and the refined atomic positions are consistent with that report, as summarized in Table I. These results indicate that the present compound crystallizes in the monoclinic space group $P2_1/c$ with lattice parameters $a = 10.47$ Å, $b = 5.01$ Å, $c = 20.37$ Å, $\alpha = \gamma = 90°$, and $\beta = 120.94°$.

The crystal structure viewed along the b axis is shown in Fig. 1(b). The Cu atoms occupy four inequivalent sites, highlighted in different colors, and partially share sites with Li^+ ions owing to the similar ionic radii of Li^+ and Cu^{2+} ions. The refined occupancies indicate that the Cu^{2+} ions occupy 30%, 46%, 49%, and 80% of the Cu1, Cu2, Cu3, and Cu4 sites, respectively (Table I). Such unavoidable site mixing has also been observed in related RS candidate Li_4CuTeO_6 [33]. Minor deviations from nominal stoichiometry in the refined Cu and Li occupancies are attributed to the high scattering

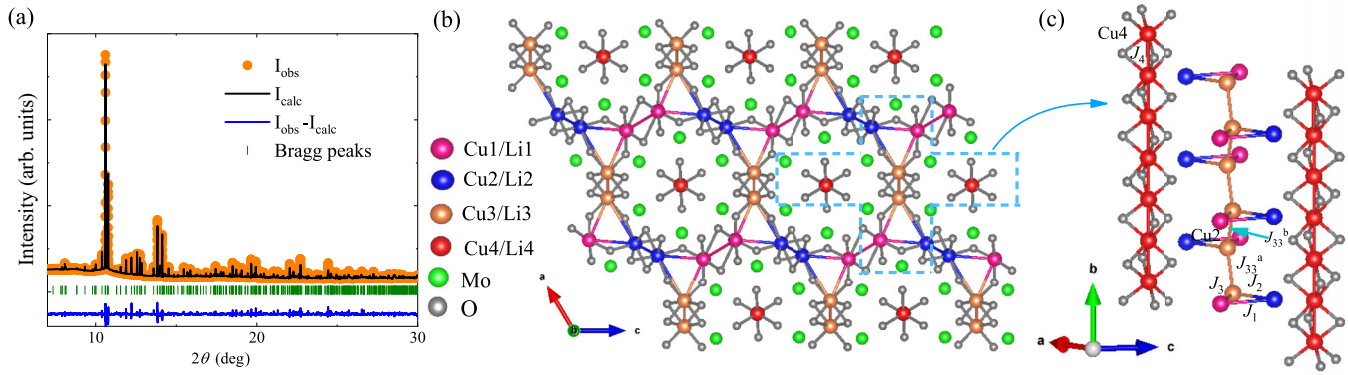

FIG. 1. (a) Synchrotron XRD pattern at 120 K together with the Rietveld refinement. Experimental data are shown as filled circles, the calculated profile as a black line, and their difference (obs–calc) as a blue line. The Bragg peak positions are marked by olive vertical bars. (b) Schematic of the 3D version of a distorted stuffed hyper-star lattice of Cu^{2+} ions projected along the *b* axis. The Cu1, Cu2, and Cu3 sites are interconnected via O ions, forming superexchange pathways of the type Cu–O–Cu. In contrast, the Cu4 site resides at the center of the polygons and is nearly isolated from the other Cu sites. (c) The dashed region in (b) is shown with the *b* axis perpendicular to the ac plane, highlighting a distorted triangular spin network of Cu^{2+} ions formed by the Cu1, Cu2, and Cu3 sites. These units are vertically connected by intertriangular bonds, generating zigzag chains of Cu ions running along the *b* axis. An example of a Cu3 chain is shown; similar chains are also formed by the Cu1 and Cu2 sites. In contrast, the Cu4 sites form a linear chain of Cu^{2+} ions.

contrast between Li and the heavier Mo and Cu ions, which places these values within the uncertainty of the synchrotron x-ray refinement. Among the Cu sites, Cu2, Cu3, and Cu4 are coordinated by CuO_6 octahedra, whereas the Cu1 site forms a distorted CuO_5 pyramid. The Cu1, Cu2, and Cu3 sites are interconnected through bridging oxygen atoms via Cu–O–Cu superexchange pathways [Fig. 1(b)]. In contrast, the Cu4 sites are relatively isolated from the other three and primarily linked through the Cu4–O–Cu4 superexchange path.

TABLE I. Atomic coordinates of $Li_2Cu_2(MoO_4)_3$ from a Rietveld refinement of synchrotron x-ray diffraction data at 120 K. ($\chi^2 = 4.57$, space group: $P2_1/c$, $a = 10.47$ Å, $b = 5.01$ Å, $c = 20.37$ Å, $\alpha = \gamma = 90°$, and $\beta = 120.94°$.)

Atom	Wyckoff position	*x*	*y*	*z*	Occ.
Mo_1	4*e*	0.315	0.713	0.344	1
Mo_2	4*e*	0.871	0.718	0.344	1
Mo_3	4*e*	0.692	1.224	0.442	1
Cu_1	4*e*	0.074	0.206	0.323	0.30
Li_1	4*e*	0.074	0.206	0.323	0.70
Cu_2	4*e*	0.953	0.751	0.525	0.46
Li_2	4*e*	0.953	0.751	0.525	0.54
Cu_3	4*e*	0.598	0.752	0.525	0.49
Li_3	4*e*	0.598	0.752	0.525	0.51
Cu_4	4*e*	0.499	0.888	0.249	0.80
Li_4	4*e*	0.499	0.888	0.249	0.20
O_1	4*e*	0.915	0.916	0.425	1
O_2	4*e*	0.436	0.913	0.425	1
O_3	4*e*	0.258	0.430	0.374	1
O_4	4*e*	0.682	0.642	0.294	1
O_5	4*e*	0.407	0.639	0.294	1
O_6	4*e*	0.9912	0.432	0.374	1
O_7	4*e*	0.164	0.931	0.288	1
O_8	4*e*	0.759	0.955	0.509	1
O_9	4*e*	0.596	1.13	0.346	1
O_{10}	4*e*	0.912	0.931	0.289	1
O_{11}	4*e*	0.846	1.428	0.460	1
O_{12}	4*e*	0.574	1.426	0.460	1

Most importantly, the superexchange pathways among the Cu1, Cu2, and Cu3 sites form a distorted 3D star lattice. In an ideal 2D star lattice, the network can be viewed as a honeycomb lattice in which each vertex is replaced by a triangle, and these triangular motifs are connected by dimer bonds branching from each vertex (see Refs. [21,22,24,34]). For a perfect 2D star lattice, the dimer bond lies flat within the plane of the triangular motifs. In contrast, in our system the dimer bonds are tilted out of the plane [e.g., J_{33}^a and J_{33}^b in Fig. 1(c)], forming finite angles with the triangles. This deviation converts the planar dimer coupling into a zigzag chain, thereby yielding a 3D hyper-star lattice.

Figure 1(c) illustrates this spin network, where two triangular motifs are connected by a zigzag chain that mediates intertriangle coupling. For clarity, only the Cu3 sites are shown; however, the Cu1 and Cu2 sites form similar zigzag chains running parallel to the *b* axis. On the other hand, the centers of the polygons constituting the hyper-star lattice are occupied by the Cu4 site, which forms an isolated chain of Cu4 ions, as depicted in Fig. 1(c), yielding a stuffed hyper-star lattice.

The resulting spin topology of the title compound can thus be regarded as a combination of two subsystems: a distorted hyper-star lattice and a uniform Cu4 spin chain located at the centers of the hyper-star lattice polygons. The bond angles and bond lengths for these sublattices are summarized in Table II. Approximate exchange interactions are inferred from structurally analogous compounds reported previously (fourth column of Table II).

Although calculating the exchange interactions in such systems is quite challenging due to site mixing, the Goodenough-Kanamori-Anderson rules together with the comparison with similar bonding geometries reveal that the intratriangular interactions J_1, J_2, and J_3 [Fig. 1(c)] with an order of magnitude of 60–90 K are significantly larger than those of the remaining

TABLE II. Cu-Cu distances, Cu–O–Cu bond angles, and corresponding exchange interactions denoted as J for $Li_2Cu_2(MoO_4)_3$. Although the absolute exchange values are not calculated, their expected magnitudes are compared with those reported for Cu-based compounds with bonding geometries.

Bond length (Å)	Bond angle (deg)	J	Expected range of J (comparative notes)
Cu1–Cu2 = 3.22	Cu1–O7–Cu2 = 106.3	J_1	$YCu_3(OH)_{6.5}Br_{2.5}$: ∠Cu–O–Cu = 112° − 116°, $J \sim 60$ K, $d_{Cu-Cu} \sim 3.3$ Å [35].
Cu1–Cu3 = 3.22	Cu1–O3–Cu3 = 106.5	J_3	
Cu2–Cu3 = 3.71	Cu2–O8–Cu3 = 120.6	J_2	$YCu_3(OH)_6Cl_3$: $\angle Cu-O-Cu = 117.8°$, $J = 87$ K, $d_{Cu-Cu} \sim 3.37$ Å [36].
Cu4–Cu4 = 2.50	Cu4–O9–Cu4 = 73.5–75	J_4	
Cu1–Cu1 = 3.60	Cu1–O7–Cu1 = 101.4	J_{11}	$Cu_2Cl(OH)_3$: $\angle Cu-O-Cu = 97.84°$, $J \sim 1.3$ K, $d_{Cu-Cu} \sim 3.01$ Å [37].
Cu2–Cu2 = 3.05	Cu2–O11–Cu2 = 94.5	J_{22}^{a}	
Cu2–Cu2 = 3.09	Cu2–O11–Cu2 = 94.5	J_{22}^{b}	$K_2Cu_3(MoO_4)_4$: $\angle Cu-O-Cu = 90.36°$, $J = 4.176$ K, $d_{Cu-Cu} \sim 3.11$ Å [38].
Cu3–Cu3 = 3.05	Cu3–O12–Cu3 = 95.9	J_{33}^{a}	
Cu3–Cu3 = 3.08	Cu3–O12–Cu3 = 94.4	J_{33}^{b}	

exchange couplings. On the other hand, the intertriangular interactions J_{22} and J_{33} are weak ferromagnetic [Fig. 1(c)]. In the absence of Li-Cu site mixing, our system may host a trimerized valence-bond crystal [26]. On the other hand, the Cu4 chain is expected to host only weak interactions, arising primarily from a competition between direct exchange across the shortest Cu4-Cu4 separation and Cu4-O-Cu4 superexchange, while the remaining couplings are likely mediated only through superexchange pathways. Thus the Cu4 subsystem may constitute weakly coupled ferromagnetic chains.

B. Magnetic susceptibility

Figure 2(a) shows the temperature dependence of the magnetic susceptibility $\chi(T)$, measured at $\mu_0 H = 0.5$ T down to 2 K. Upon lowering the temperature, $\chi(T)$ increases monotonically, without any clear signature of long-range magnetic ordering. The low-temperature upturn is attributed to contributions from weakly coupled spins or orphan spins arising from magnetic-site vacancies in LCMO [39]. This interpretation is further supported by the nonlinear behavior of the isothermal magnetization at low temperatures, as discussed below.

To determine the dominant magnetic exchange interactions, the temperature dependence of the inverse magnetic susceptibility $1/\chi(T)$ is plotted in Fig. 2(b) after subtracting the total diamagnetic contribution from all ions, $\chi_{dia} = -2.3 \times 10^{-3}$ cm^3/mol [40]. The high-temperature linear region of $1/\chi(T)$ follows a Curie-Weiss (CW) law, $\chi = \chi_{VV} + C/(T - \theta_{CW})$, where $\chi_{VV} = 1.78 \times 10^{-4}$ cm^3/mol is

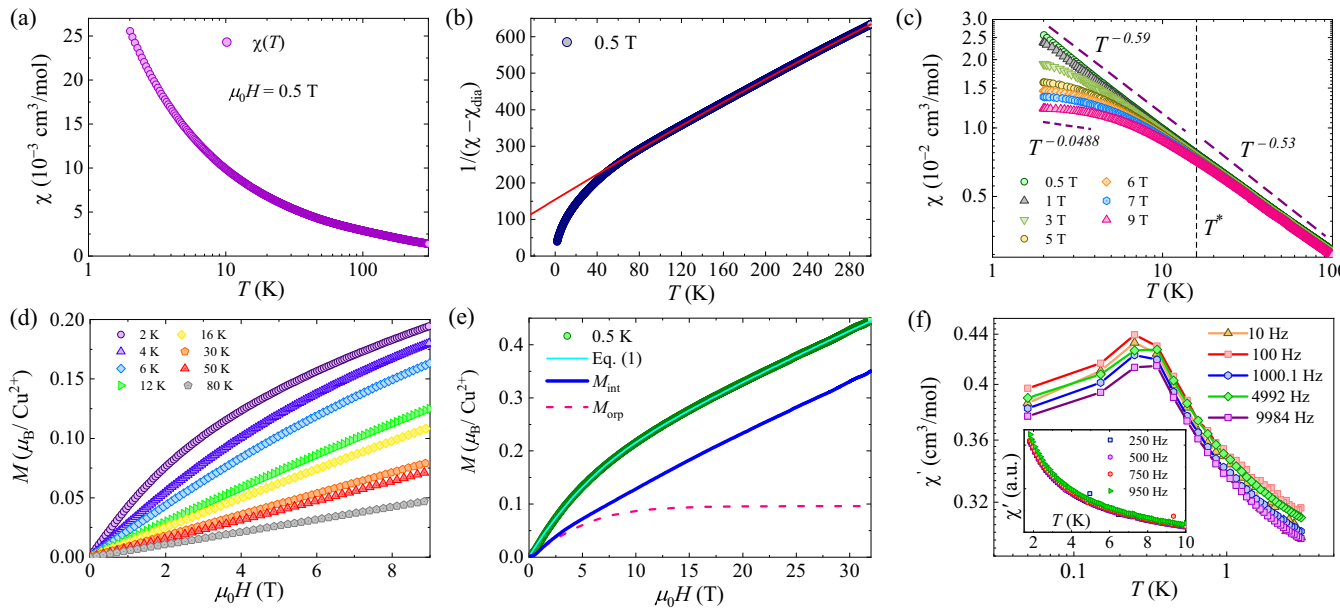

FIG. 2. (a) Temperature-dependent magnetic susceptibility $\chi(T)$ of $Li_2Cu_2(MoO_4)_3$ at $\mu_0 H = 0.5$ T. (b) Temperature dependence of the inverse magnetic susceptibility after subtracting the diamagnetic contribution. The high-temperature Curie-Weiss fit is shown by a red line. (c) Log-log plot of $\chi(T)$ at various magnetic fields. The dashed vertical line (black) indicates the position of $T^* = 15.8$ K. Above and below T^*, $\chi(T)$ follows a power-law behavior, as indicated by the dashed lines (purple). (d) Isothermal magnetization at various temperatures. (e) High-field magnetization data decomposed into intrinsic magnetization M_{int} and orphan-spin contribution M_{orp} using Eq. (1), as described in the text. (f) Real part of the ac magnetic susceptibility at various frequencies in the low-temperature range. The inset shows the data above 2 K for lower frequencies.

the temperature-independent Van Vleck susceptibility, $C = 0.54\,\mathrm{cm^3\,K/mol}$ is the Curie constant, and $\theta_{\mathrm{CW}} = -85.76$ K is the CW temperature. The large negative value of θ_{CW} indicates dominant antiferromagnetic interactions in LCMO. The effective magnetic moment was estimated as $\mu_{\mathrm{eff}} = \sqrt{8C} = 2.07\mu_{\mathrm{B}}$, corresponding to $s = 1/2$ moment with a Landé g factor of 2.39. Below 80 K, the experimental data deviate from the CW behavior, implying the development of antiferromagnetic spin correlations, as further supported by the magnetic specific heat discussed in Sec. III C.

As discussed in Sec. III A, the system comprises two distinct spin topologies. To clarify which topology, either the 3D hyper-star lattice or the Cu4 spin chain, dominates the antiferromagnetic interactions, we performed DFT calculations accounting for possible Cu-Li site mixing. In these calculations, Cu4 and Cu1 sites were assumed to be fully occupied by Cu^{2+} ions, while Li2 and Li3 sites were occupied by Li^{+} ions to maintain charge neutrality according to the stoichiometric formula unit. Using this configuration, DFT calculations with an on-site Hubbard parameter of $U = 6$ eV yield an exchange interaction strength of $J_4 \approx 1.28$ K (Cu4–Cu4), corresponding to an approximate CW temperature of $\theta_{\mathrm{CW}}^{\mathrm{chain}} \approx -0.64$ K within the mean-field approximation. However, the experimentally observed large negative $\theta_{\mathrm{CW}} = -85.76$ K suggests that the dominant antiferromagnetic exchange originates from the hyper-star lattice spin topology rather than from the spin-chain network. The exchange interactions within the hyper-star lattice were not explicitly calculated, as site mixing and the associated charge-balance constraints among the Cu1, Cu2, and Cu3 sites introduce considerable complexity. Notwithstanding, we recall that the qualitatively deduced exchange interactions of $J_1, J_2, J_3 \sim 60$–90 K match well with the CW temperature.

Figure 2(c) displays the temperature dependence of $\chi(T)$ at various magnetic fields below 100 K. Upon cooling below $|\theta_{\mathrm{CW}}|$, $\chi(T)$ follows a $T^{-0.53}$ power-law behavior down to $T^* = 15.8$ K with weak field dependence. This sub-Curie $\chi(T)$ increase alludes to the presence of random exchange interactions. At lower temperatures, a steeper power-law increase of $T^{-0.59}$ at 0.5 T signals enhanced RS-like behavior, possibly due to the increasingly enhanced contribution of weakly interacting spins, resulting in a broader distribution of exchange interactions. While $\chi(T)$ above T^* remains nearly field independent, below T^* it shows strong field dependence, with the exponent evolving from 0.59 at 0.5 T to 0.048 at 9 T, implying a progressive quenching of weakly coupled RS with increasing magnetic fields.

To further confirm the existence of randomly interacting spins in LCMO, the isothermal magnetization $M(H)$ was measured at several temperatures, as shown in Fig. 2(d). Above T^*, $M(H)$ displays a linear field dependence, consistent with $T < |\theta_{\mathrm{CW}}|$. In contrast, below T^*, the magnetization deviates from linearity without exhibiting any hysteresis, witnessing the subdominant yet finite contribution of orphan spins. Throughout this paper, orphan spins in the RS context collectively refer to weakly coupled paramagnetic or defect spins and vacancy-induced quasispins.

High-field magnetization measurements up to 35 T were conducted to examine possible field-induced correlated states in this magnetic site diluted 3D system [26]. As illustrated in Fig. 2(e), the magnetization reaches $0.45\mu_{\mathrm{B}}$ at 31 T, whose extrapolation yields the expected full saturation value of $1\mu_{\mathrm{B}}$ at fields close to 85 T, in accord with $|\theta_{\mathrm{CW}}|$. Although ideal 2D star lattices are predicted to host field-induced correlated states, such features are absent in the present system, likely due to the interplay of 3D exchange interactions and intrinsic magnetic site disorder [26]. In line with the low-field observations below T^* [Fig. 2(d)], the nonlinear magnetization $M(H)$ at 0.5 K [Fig. 2(e)] is governed by orphan spins and its concentration can be determined by using the following phenomenological model [41,42],

$$M(H) = \frac{\eta_{\mathrm{orp}} g \mu_B}{2} \tanh\left[\frac{g\mu_B\mu_0 H}{k_B(T-\theta^*_{\mathrm{orp}})}\right] + A(\mu_0 H)^n, \quad (1)$$

where the first term represents a modified Brillouin function describing the magnetization of weakly interacting orphan spins, while the second term captures the power-law field dependence arising from random exchange interactions [3,4,42]. In Eq. (1), η_{orp} refers to the number of orphan spins, μ_{B} is the Bohr magneton, g denotes the Landé g factor, and θ^*_{orp} represents the effective interaction energy scale between orphan spins, while A and n are fitting parameters. The solid cyan line in Fig. 2(e) represents the fits obtained using Eq. (1) assuming $g = 2$, and the corresponding parameters yield $\eta_{\mathrm{orp}} = 9.63(1)\%$, $\theta^*_{\mathrm{orp}} = -8.52(1)$ K, $n = 0.853(2)$, and $A = 0.0181(2)$. The obtained exponent $n = 0.853$, which is smaller than 1, reflects the contribution arising from randomness in the exchange interactions [4], and may be indicative of RS-like correlations.

In systems with quenched disorder, spin freezing often emerges at low temperatures. To inspect whether such freezing occurs in the present case, we performed frequency-dependent ac magnetic susceptibility measurements over a wide temperature range. The data between 2 and 10 K are shown in the inset of Fig. 2(f). The absence of any frequency dependence rules out spin freezing down to 2 K. In contrast, the low-temperature ac magnetic susceptibility data collected between 0.05 and 3.4 K [Fig. 2(f)] reveal a cusp around $T_f \approx 0.3$ K. With increasing frequency, this cusp shifts to higher temperatures, indicating that partial spin freezing takes place.

C. Specific heat

In order to confirm the absence of long-range magnetic order and probe low-energy magnetic excitations across different energy scales, specific-heat measurements were carried out down to 0.2 K. Figure 3(a) presents the temperature dependence of the specific heat at several magnetic fields. The absence of a λ-type anomaly rules out any thermodynamic phase transition in LCMO down to the lowest measured temperature.

In general, the specific heat $C_p(T)$ in magnetic insulators comprises three contributions, namely, the magnetic, lattice, and Schottky terms relevant under finite fields. Given the unavailability of a nonmagnetic analog of LCMO, the lattice contribution was determined by fitting the data [solid red line in Fig. 3(a)] with a model comprising one Debye and

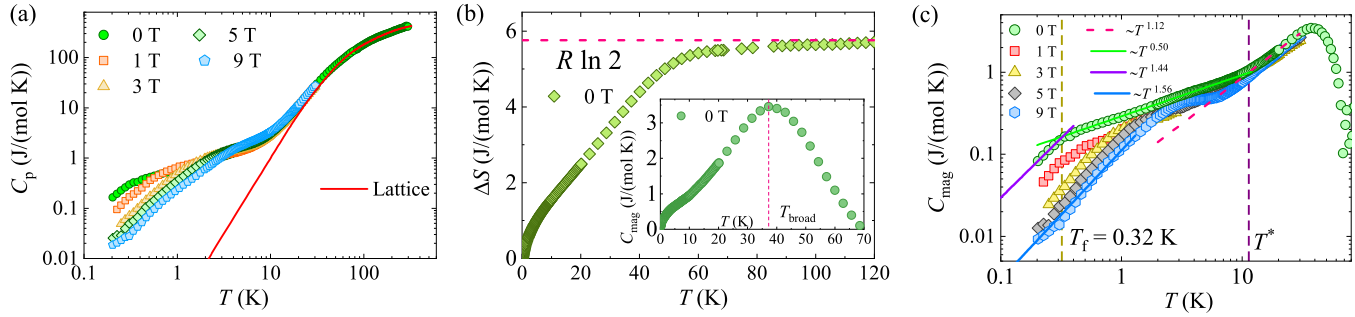

FIG. 3. (a) Temperature dependence of the specific heat at several magnetic fields, where the solid red line corresponds to the lattice contribution. (b) Magnetic entropy as a function of temperature at zero field. The dashed pink horizontal line indicates the expected entropy $R \ln 2$ for an $s = 1/2$ system. The inset shows the magnetic specific heat as a function of temperature. (c) Log-log plot of the magnetic specific heat as a function of temperature at various magnetic fields. In zero field, three distinct power-law regimes below the broad maximum are identified, as indicated in the legend, and separated by dashed vertical lines at $T^* = 11.11$ K and $T_f = 0.32$ K.

three Einstein terms, i.e.,

$$C_{\text{latt}}(T) = C_D\left[9R\left(\frac{T}{\theta_D}\right)^3 \int_0^{\theta_D/T} \frac{x^4 e^x}{(e^x-1)^2}\,dx\right] + \sum_{i=1}^{3} C_{E_i}\left[R\left(\frac{\theta_{E_i}}{T}\right)^2 \frac{e^{\theta_{E_i}/T}}{(e^{\theta_{E_i}/T}-1)^2}\right], \quad (2)$$

where $\theta_D = 180 \pm 6$ K is the Debye temperature, and $\theta_{E_1} = 282 \pm 2$ K, $\theta_{E_2} = 293 \pm 4$ K, and $\theta_{E_3} = 751 \pm 8$ K represent the Einstein temperatures of three optical phonon modes, with R being the molar gas constant. To minimize the number of free parameters, C_D was set to 3, corresponding to the three acoustic phonon modes. The best fit is obtained with $C_{E_1} = 4$, $C_{E_2} = 5$, and $C_{E_3} = 10$, which together account for the 54 optical phonon modes expected from the $(3n - 3)$ branches for $n = 19$ atoms in LCMO [43].

After subtracting the lattice contribution, the resulting magnetic specific heat $C_{\text{mag}}(T)$ is presented in the inset of Fig. 3(b). $C_{\text{mag}}(T)$ increases below 70 K and displays a broad maximum near 40 K, suggesting the presence of short-range spin correlations arising from antiferromagnetic Heisenberg interactions in the hyper-star lattice spin network [44]. We note that a deviation from the CW fit emerges below 80 K, which coincides with the growth of $C_{\text{mag}}(T)$ below 70 K. The change in magnetic entropy was determined by integrating $C_{\text{mag}}(T)/T$, as shown in Fig. 3(b). The total entropy recovered near the CW temperature is ~5.67 J/(mol K), in good agreement with the expected $R \ln(2S + 1)$ for an $s = 1/2$ system.

Figure 3(c) depicts the temperature dependence of $C_{\text{mag}}(T)$ at various magnetic fields after subtracting the Schottky contribution (see the Appendix). The coexistence of distinct energy scales associated with the two sublattices is particularly evident in the zero-field data. For instance, below the broad maximum, $C_{\text{mag}}(T)$ follows an almost linear $T^{1.12}$ dependence, terminating near $T^* \approx 11.1$ K, indicative of low-energy gapless excitations that persist down to T^*. At lower temperatures, $C_{\text{mag}}(T)$ evolves into a $T^{0.50}$ dependence over the range 0.32–11.1 K, pointing to the prevailing contributions of a RS-like state, consistent with $\chi(T) \sim T^{-0.59}$ behavior below T^*. Upon further cooling ($T < 0.32$ K), $C_{\text{mag}}(T)$ undergoes a curvature change, approaching a $T^{1.44}$ dependence. This crossover coincides with the spin-freezing transition observed in the ac magnetic susceptibility at $T_f \approx 0.32$ K, below which quasifrozen states manifest through a subquadratic temperature dependence. As the magnetic field increases, the subtle low-temperature slope below 0.32 K weakens progressively, indicating the suppression of the quasifrozen state while retaining the subquadratic temperature dependence characteristic of exotic gapless excitations, which persists even up to 9 T.

Note that the characteristic temperature T^* identified from $C_{\text{mag}}(T)$ is slightly lower than that observed in $\chi(T)$ and other microscopic experiments ($T^* = 15.8$ K) discussed below. This difference likely arises from the varying sensitivities of the experimental probes. However, we consider $T^* = 15.8$ K as the reference value derived from microscopic measurements.

D. Electron spin resonance

To further elucidate the thermal evolution of spin-spin correlations, we performed X-band ESR measurements down to 3.8 K. As shown in Fig. 4(a), the ESR spectra recorded at various temperatures are well reproduced by a derivative of a Lorentzian curve. The ESR spectra exhibit pronounced broadening at high temperatures, followed by gradual narrowing as the temperature decreases. For $T > 60$ K, the linewidth becomes too broad to be resolved within the X-band frequency window.

As the ESR linewidth reflects the combined effects of spin-spin and spin-lattice relaxation, its temperature evolution, as captured by the ESR linewidth $\Delta H_w(T)$, provides valuable information on the underlying spin dynamics, as illustrated in Fig. 4(b). Upon lowering the temperature below 60 K, ΔH_w decreases gradually, following a power-law dependence, $\Delta H_w \propto T^{0.25}$, down to $T^* = 15.8$ K. For $T \gg J$, the ESR linewidth is usually expected to remain temperature independent. However, the observed anomalous temperature dependence indicates the influence of spin-spin correlations and spin-lattice coupling. Furthermore, in transition metal based compounds, the spin-lattice relaxation contribution to the ESR linewidth typically leads to either an increase with temperature (via direct or Raman processes) or a saturation

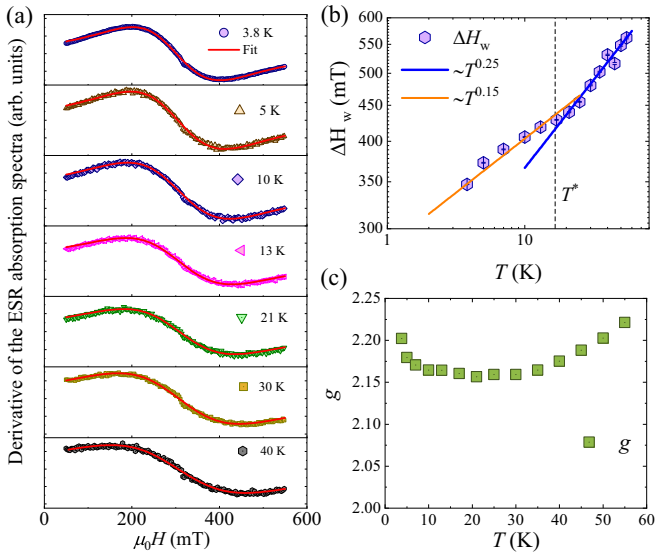

FIG. 4. (a) Derivative of the ESR absorption spectra of $Li_2Cu_2(MoO_4)_3$ at selected temperatures where the Lorentzian lineshape fitting is shown by the solid red lines. (b) Temperature dependence of the ESR linewidth ΔH_w that shows a crossover in its power-law dependence across $T^* = 15.8$ K (dashed vertical line). (c) Temperature dependence of the g factor, exhibiting a nonmonotonic variation.

at low temperatures [45]. The sublinear narrowing observed here cannot be accounted for by conventional spin-lattice relaxation. Instead, it points to the dominant role of spin-spin relaxation processes, possibly associated with static short-range order in low-dimensional magnets [46].

Below T^*, the linewidth exhibits a further decrease, following a different power-law trend of $\sim T^{0.15}$, indicating the onset of another correlated regime. Unlike the inhomogeneous broadening commonly observed in RS candidates [47], the present system exhibits a two-stage power-law narrowing of the ESR linewidth upon cooling. A similar two-step linewidth evolution has been reported for the alternating kagome bilayer compound $Ca_{10}Cr_7O_{28}$ [48], where it was attributed to the emergence of two magnetic sublattices with distinct correlation strengths. In the gigahertz frequency window, the spin dynamics appears to be dominated by exotic spin correlations, rather than inhomogeneous RS spin dynamics.

Figure 4(c) shows a weakly nonmonotonic temperature dependence of the g factor ($\approx 2.15 - 2.20$), exhibiting a shallow minimum around T^* and slight upturns at both lower and higher temperatures. Notably, $C_{\rm mag}(T)$ changes its power-law behavior around T^*, closely aligning with the g factor minimum. Throughout the measured temperature range, the effective g value remains typical of Cu^{2+}-based systems with a quenched orbital moment [49]. In exchange-coupled insulating magnets, the variation of g on both sides of the minimum indicates a crossover in spin-spin correlations, consistent with the changes observed in the linewidth and $C_{\rm mag}(T)$ around T^*.

Altogether, the intratriangular spin correlations progressively evolve into a more RS-like state that coexists with spin-chain correlations as weak residual interactions become relevant at lower temperatures.

E. Muon spin relaxation

To further investigate the low-energy spin dynamics associated with magnetic site dilution, μSR measurements were performed down to 2 K. μSR is a highly sensitive local probe, in which fully polarized positive muons are implanted into the sample to monitor the microscopic spin dynamics through the time evolution of the muon spin polarization [50].

Figure 5(a) depicts the time evolution of the normalized muon spin polarization at various temperatures in ZF. A slow relaxation is observed between 2 and 120 K; however, the absence of coherent oscillations indicates the lack of long-range magnetic order at least down to 2 K. Moreover, no indication of a "1/3" tail in the ZF asymmetry further rules out any conventional spin freezing for $T \geqslant 2$ K, consistent with thermodynamic results [51].

The ZF spectra are well modeled by the following polarization function [solid lines in Fig. 5(a)],

$$P(t) = \exp\left[-\tfrac{1}{2}(\sigma_{\rm ZF}t)^2\right]\exp(-\lambda_{\rm ZF}t),$$

where the Gaussian term accounts for the static nuclear dipolar fields characterized by the relaxation rate $\sigma_{\rm ZF}$, while the exponential term represents the slow relaxation of electronic origin with the muon spin relaxation rate $\lambda_{\rm ZF}$. A comparable muon spin polarization, arising from the combined effects of nuclear dipolar fields and electronic spins, has been observed in the Li-Cu site-mixing RS candidate Li_4CuTeO_6 [33].

The estimated $\lambda_{\rm ZF}$ is shown in Fig. 5(b) as a function of temperature. In most 3d transition-metal compounds, the ZF muon spin relaxation rate of electronic origin provides a measure of spin-spin correlations. In LCMO, above $T^* = 15.8$ K, $\lambda_{\rm ZF}$ exhibits only a weak temperature dependence, following a $T^{0.26}$ power-law behavior, which signals the persistence of characteristic spin-spin correlations at elevated temperatures. Consistently, the ESR linewidth also follows a $T^{0.25}$ dependence above T^*. Such weak power-law behavior ($\lambda_{\rm ZF} \sim T^{0.26}$ and ESR linewidth $\sim T^{0.25}$) is often reported in 1D Luttinger liquids and 2D frustrated magnets hosting specific spinons [52], and in LCMO this correlated regime extends down to T^*.

Upon further cooling below T^*, $\lambda_{\rm ZF}$ begins to increase and follows a distinct power-law behavior, $\lambda_{\rm ZF} \sim T^{-0.57}$. Notably, this growth of $\lambda_{\rm ZF}(T)$ is opposite to the ESR linewidth narrowing, highlighting the frequency-dependent spin dynamics. In the MHz time window, the influence of quenched disorder and associated localized orphan spin becomes more prominent [15]. These vacancy-induced orphan spins, most likely originating from Li-Cu site mixing in LCMO, interact with the surrounding bulk spins in a highly inhomogeneous manner. As such, slow spin dynamics dominated by vacancy-induced orphan spins is responsible for the low-temperature power-law enhancement of $\lambda_{\rm ZF}$ [9,20].

Figure 5(c) shows the temperature dependence of the Gaussian relaxation rate, which remains nearly temperature independent over the measured temperatures, reflecting the maximum width of the static nuclear field distribution of about $\sim$2 Oe. To confirm that this Gaussian relaxation originates from nuclear dipolar fields, we performed LF-μSR measurements at 2 K, as shown in Fig. 5(d). Upon increasing the applied LF beyond the static nuclear field ($\gg 2$ Oe), the muon spin relaxation progressively decouples from the static nuclear

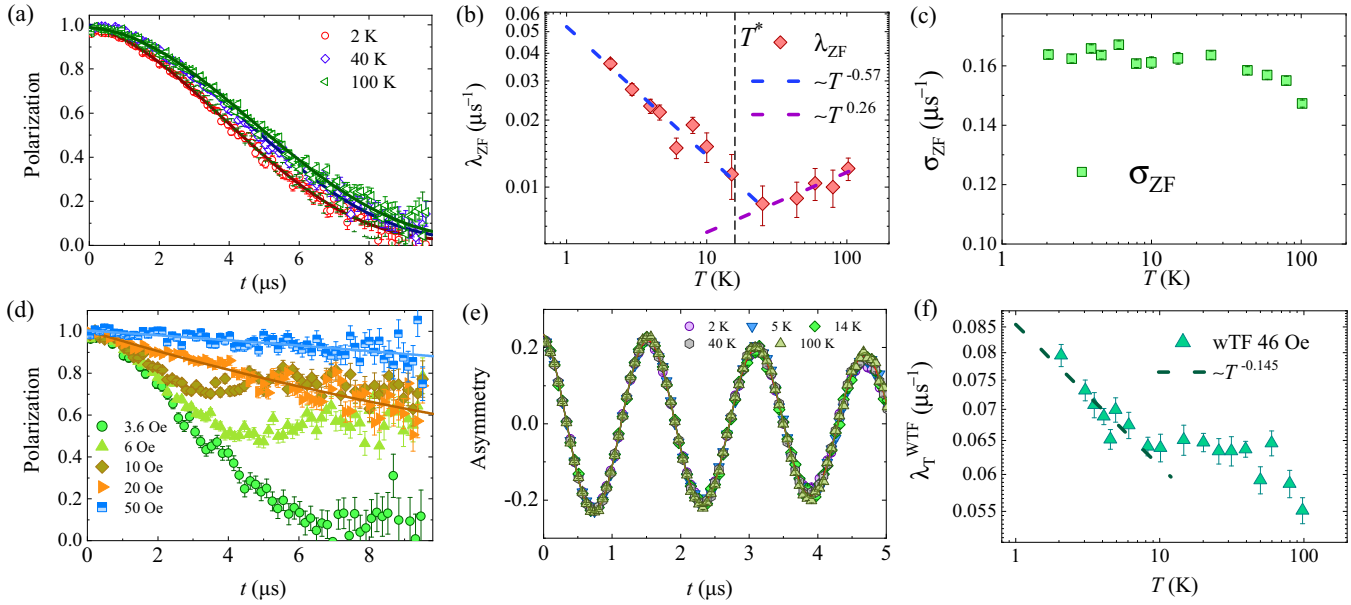

FIG. 5. (a) Time evolution of normalized muon spin polarization in zero field at three temperatures. (b), (c) Temperature dependence of the muon spin relaxation rate of electronic origin (λ_{ZF}) and nuclear origin (σ_{ZF}). The dashed lines indicate the crossover in spin-spin correlations across $T^* = 15.8$ K, highlighting distinct power-law regimes as discussed in the text. (d) Time evolution of normalized muon spin polarization in several longitudinal fields at 2 K. (e) Time dependence of muon spin asymmetry at a weak-transverse field $H_{TF} = 46$ Oe at several temperatures. (f) Temperature dependence of the transverse relaxation rate extracted from weak transverse-field measurements.

fields. At around 20 Oe (≈10 times that of the nuclear field), a nearly complete decoupling is achieved, leaving only a weak exponential relaxation component of electronic origin. The solid lines in Fig. 5(d) represent fits using the simple exponential polarization function $P(t)_{LF} = \exp(-\lambda_{LF}t)$, which yield the relaxation rates of $\lambda_{LF} = 0.013$ μs^{-1} at 20 Oe and 0.0023 μs^{-1} at 50 Oe. Notably, even under fields exceeding the static nuclear field by more than an order of magnitude, a finite muon spin relaxation persists, evidencing the presence of slow electronic spin fluctuations at low temperatures.

To further investigate the low-temperature spin dynamics, we carried out wTF-μSR measurements at several temperatures. Figure 5(e) presents the time evolution of the muon spin asymmetry in an external field of $H_{TF} = 46$ Oe, applied perpendicular to the initial direction of muon spin polarization. In this geometry, the muon spins precess coherently around the transverse field H_{TF}. As the applied field is much larger than the width of the static nuclear field obtained from ZF, the observed relaxation beyond the nuclear contribution must stem from paramagnetic spins, in line with the ZF data that show no evidence of static electronic fields. As evident from Fig. 5(e), the full asymmetry (A_0) persists down to 2 K, confirming the lack of static electronic fields in agreement with the ZF data. To analyze the wTF spectra, we employed a damped oscillatory function,

$$A_{wTF}(t) = A_0 \cos(\gamma_\mu H_{TF} t + \phi) e^{-\lambda_{TF} t}, \quad (3)$$

in which the muon spins precess at frequency $\omega = \gamma_\mu H_{TF}$, ϕ represents the phase shift, and λ_{TF} quantifies the relaxation rate arising from slow spin fluctuations of electronic origin.

The temperature dependence of the transverse relaxation rate λ_{TF} is shown in Fig. 5(f). For $T > T^*$, λ_{TF} remains nearly temperature independent, reflecting the response of randomly oriented paramagnetic spins. In contrast, a pronounced enhancement appears between 2 and 10 K, indicating the presence of a crossover regime that may be related to the correlated orphan spins behavior inferred from the ZF measurements. A direct comparison reveals that the ZF relaxation rate λ_{ZF} [Fig. 5(b)] is weaker than the transverse field relaxation rate λ_{TF} [Fig. 5(f)]. This is related to the fact that while the ZF relaxation reflects only dynamic field fluctuations, the transverse relaxation is additionally affected by inhomogeneous local fields induced by the applied transverse field. Furthermore, the overall temperature dependence of λ_{TF} ($\sim T^{-0.14}$) is weaker than that of λ_{ZF} ($\sim T^{-0.57}$), possibly due to partial quenching of weakly coupled spin dynamics by the applied transverse field.

IV. DISCUSSION

Vacancy-induced quenched disorder presents fundamental challenges in understanding correlated quantum states. In the present compound, Li-Cu site mixing introduces intrinsic disorder that perturbs the exchange network of the clean hyper-star lattice while largely preserving its frustrated character.

It is noteworthy that despite the substantial Li-Cu site mixing, the system does not appear to reside at a magnetic percolation threshold. Instead, the Cu^{2+} moments form an extended, randomly connected 3D network that effectively fragments into low-dimensional magnetic segments. In this geometry, the primary source of frustration associated with the ideal triangular plaquettes is mostly suppressed. Nevertheless, residual frustration may persist due to bond disorder induced random exchange interactions, which are well established as a driver of spin frustration in 1D RS systems [53].

At high temperatures, dominant antiferromagnetic correlations originate from strong yet diluted intratriangle exchange interactions. Upon cooling, a RS-like state develops through a distribution of intertriangle exchange couplings and weakly interacting Cu4 spin chains. Ultimately, the spins undergo progressive freezing driven by the residual 3D exchange interactions linking the hyper-star lattice and the Cu4 chain network.

The dominance of antiferromagnetic intratriangle interactions and the emergence of an orphan spins driven RS-like state are manifested in the $\chi(T)$ data. In the temperature range 15–100 K, $\chi(T)$ remains nearly field independent and follows a power-law behavior $\chi(T) \sim T^{-0.53}$, consistent with random magnetism dominated by the magnetic segment coupled by intratriangle antiferromagnetic interactions [54]. At lower temperatures, however, the growing contribution from weak residual interactions enhances the magnetic susceptibility through a distribution of exchange interactions, as reflected by $\chi(T) \sim T^{-0.59}$ below T^*. With increasing magnetic field, the low-temperature susceptibility is drastically modified, as reflected by the change of the exponent from 0.59 to 0.0488, implying a gradual polarization of the orphan spins under applied fields below T^*. The spin dynamics arising from low dimensionally segmented antiferromagnetic interactions at high temperatures are further corroborated by the broad maximum in $C_{\mathrm{mag}}(T)$ [55], along with the power-law behavior of the ESR linewidth and the zero-field muon spin relaxation rate above T^*, indicating the development of short-range spin correlations typical of low-dimensional Heisenberg antiferromagnets [55].

Before discussing further evidence for an intermediate RS-like state below T^*, it is worth noting that, despite the presence of both vacancy and bond disorder, we do not observe a clear $\chi(T) \propto C/T$ Curie tail at low temperatures. Such behavior is commonly seen in 1D systems, where it often originates from extraneous orphan spins [39]. In our case, the magnetization data indicate that orphan spins do exist, but they are an intrinsic feature of the site-diluted system rather than isolated paramagnetic impurities [15,56]. Instead of producing a simple $1/T$ divergence, these orphan spins are weakly correlated in the random-bond background, forming singlets of varying energy scales. This redistribution of exchange energy suppresses the Curie-like tail and drives the system toward a RS-like state, characterized by $\chi(T) \sim T^{-\alpha}$, $C_{\mathrm{mag}}(T) \sim T^{1-\alpha}$, and $\lambda_{\mathrm{ZF}}(T) \sim T^{-\alpha}$, where the low-energy density of states follows $D(E) \propto E^{-\alpha}$ [9,12,13,57].

In addition to the power-law behavior of $\chi(T)$, the magnetic specific heat below T^* follows $C_{\mathrm{mag}}(T)/T \sim T^{-0.5}$ down to $T_f = 0.32$ K, marking the lowest temperature of the RS-like state (see Table III). This behavior is further corroborated microscopically by the muon spin relaxation rate, $\lambda_{\mathrm{ZF}} \sim T^{-0.57}$. Notably, the exponents derived from both thermodynamic and microscopic probes lie within a similar range, offering strong evidence for the emergence of a RS-like state in the intermediate temperature window between T_f and T^* in zero field. It is worth noting that within the gigahertz frequency regime, the spin dynamics is dominated by unconventional spin correlations, whereas the inhomogeneous RS-type fluctuations observed at megahertz frequencies remain unresolved (see Table III).

TABLE III. Temperature-dependent power-law behavior for various physical quantities in $Li_2Cu_2(MoO_4)_3$.

Physical quantity	Intratriangle ($T > T^*$)	Random singlet ($T_{\mathrm{f}} < T < T^*$)
$\chi(T)$	$T^{-0.53}$	$T^{-0.59}$
$C_{\mathrm{mag}}(T)/T$	$T^{0.12}$	$T^{-0.50}$
$\lambda_{\mathrm{ZF}}(T)$ (MHz)	$T^{0.26}$	$T^{-0.57}$
$\Delta H_w(T)$ (GHz)	$T^{0.25}$	$T^{0.15}$
Quasifrozen regime: $T < T_{\mathrm{f}}$, $C_{\mathrm{mag}}(T)/T \propto T^{0.44}$		

We recall that singlets initially form on the shortest and strongest bonds, while spins connected by longer or weaker bonds remain effectively unpaired at higher temperatures. Upon further lowering the temperature, singlet formation extends over increasing length scales, resulting in a reduced fraction of weakly coupled orphanlike local moments that nevertheless dominate the low-energy magnetic response. Importantly, this implies a thermal redistribution of spectral weight between orphan-spin and singlet-spin contributions.

To further examine the scenario of the RS state in applied magnetic fields, Fig. 6 presents the scaling analysis of $\chi(T)$, $M(H)$, and $C_{\mathrm{mag}}(T)$, commonly proposed as hallmarks of a disorder-induced RS-like state [8,11,14]. In Fig. 6(a), the scaled form $\mu_0 H^{0.56}\chi(T)$ collapses onto a universal curve when plotted against $T/\mu_0 H$, consistent with RS scaling behavior. Although the exponent $\alpha_\chi = 0.56$ is close to that expected near zero-field condition ($\alpha = 0.50$ to 0.59), the scaling of $T^{-0.45}M$ versus $\mu_0 H/T$ [Fig. 6(b)] produces a single curve over 2–80 K with a complementary exponent ($\alpha_M \sim 1 - \alpha_\chi$). Furthermore, the low-temperature specific heat measured in various magnetic fields collapses as $\mu_0 H^{0.25} C_{\mathrm{mag}}(T)/T$ versus $T/\mu_0 H$, yielding an exponent $\alpha_C = 0.25$ even lower than that extracted from zero-field data [Fig. 6(c)]. These observations suggest that, although scaling collapse is retained under magnetic fields, the exponents differ substantially from their zero-field counterparts. A similar trend is found in the collapse behavior of thermodynamic quantities in Y_2CuTiO_6 [11]. Unlike in 1D RS systems, disorder-driven singlet formation in higher-dimensional frustrated magnets is expected to exhibit nonuniversal effective exponents. Moreover, both the existence and the universality of a well-defined 3D RS state remain open questions. The 1 T data are intentionally excluded from the scaling plot in Fig. 6(c), as satisfactory data collapse is observed only for higher magnetic fields (3–9 T), similar to what has been reported for the 3D RS candidate Li_4CuTeO_6 [33].

Although in the intermediate temperature range the system exhibits a RS-like state, at lower temperatures around $T_f = 0.32$ K it undergoes spin freezing, as revealed by the ac magnetic susceptibility measurements. Notably, this freezing occurs only at very low temperatures, suggesting an origin in the Cu4 spin chains, where the Cu4–Cu4 coupling ($J_4 = 1.23$ K) drives a quasifrozen state within the dominant RS background set by the 3D hyper-star lattice spin topology. Under magnetic fields, however, this quasifrozen contribution is gradually suppressed, and by 9 T the magnetic specific heat recovers a quadratic dependence, consistent with low-energy gapless excitations [58].

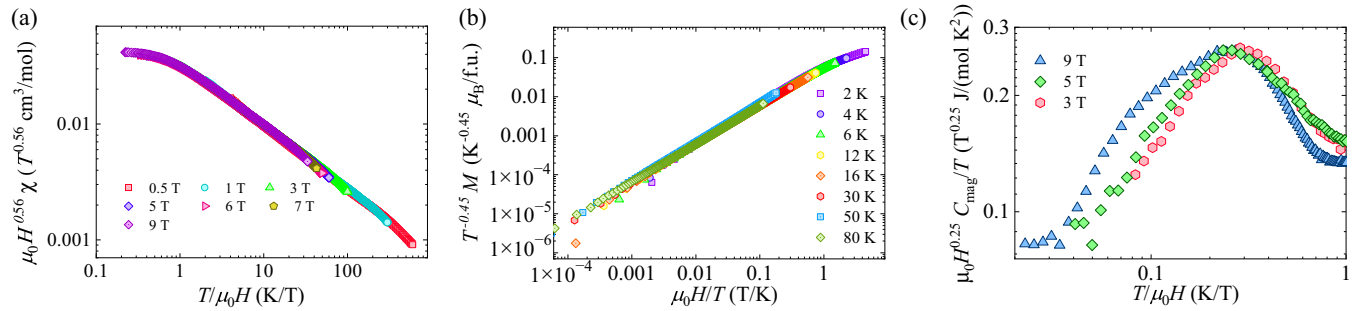

FIG. 6. (a) Magnetic susceptibility $\chi(T)$ rescaled by magnetic field $\mu_0 H^{0.56}$ and plotted against $T/\mu_0 H$, showing data collapse onto a universal-like curve. (b) Isothermal magnetization M multiplied by $T^{-0.45}$ as a function of $\mu_0 H/T$, demonstrating consistent scaling over a wide temperature range. (c) Scaled magnetic specific heat $\mu_0 H^{0.25} C_{\mathrm{mag}}/T$ vs $T/\mu_0 H$ at selected fields, highlighting collapse onto a common trend. All panels are presented in a log-log scale.

V. CONCLUSION

In summary, thermodynamic and microscopic measurements identify $Li_2Cu_2(MoO_4)_3$ as a rare 3D hyper-star lattice, where Li-Cu site disorder drives a crossover from antiferromagnetic short-range correlations at high temperatures to a RS-like state at low temperatures. The broad maximum in $C_{\mathrm{mag}}(T)$ and power-law behaviors of the muon relaxation rate and ESR linewidth ($T^{0.26}$) above $T^* \approx 15.8$ indicate dominant short-range correlations characteristic of low-dimensional antiferromagnets. Below T^*, orphan spins with weak random interactions produce distinct power-law dependences in various physical observables ($T^{-0.50}$) with comparable exponents, evidencing a RS-like state. The universal scaling of $\chi(T)$, $M(H)$, and $C_{\mathrm{mag}}(T)$ under field supports this scenario, while varying exponents indicate an intriguing nature of the higher-dimensional RS state. Upon further cooling, a quasifrozen state emerges near $T_f = 0.32$ K, likely from weakly coupled Cu4 spin chains. Altogether, $Li_2Cu_2(MoO_4)_3$ reveals that site disorder in a 3D frustrated lattice can intertwine bulk and orphan spins, giving rise to an extended RS-like quantum-disordered state beyond two dimensions.

ACKNOWLEDGMENTS

The work at SKKU was supported by the National Research Foundation (NRF) of Korea (Grants No. RS-2023-00209121 and No. 2020R1A5A1016518). S.M.K. and C.-L.H. are supported by the National Science and Technology Council in Taiwan with Grant No. NSTC 114-2112-M-006-012. R.S. acknowledges the financial support provided by the Ministry of Science and Technology in Taiwan under Projects No. NSTC-114-2124-M-001-009 and No. NSTC-113-2112M001-045-MY3, as well as support from Academia Sinica for the budget of AS-iMATE11512. We also acknowledge financial support from the Center of Atomic Initiative for New Materials (AIMat), National Taiwan University, under Project No. 113L900801.

DATA AVAILABILITY

The data that support the findings of this article are openly available [59].

APPENDIX: SPECIFIC HEAT

Figure 7(a) shows the residual specific heat after subtraction of the lattice contribution. The zero-field data are free from any field-induced Schottky contribution, which typically arises under applied magnetic fields due to Zeeman splitting of $s = 1/2$ orphan spins or spin singlets. In zero field, the data exhibit three distinct power-law regimes in temperature, reflecting successive changes in spin correlations upon cooling. With increasing magnetic field, the narrow low-temperature slope below 0.32 K gradually decreases,

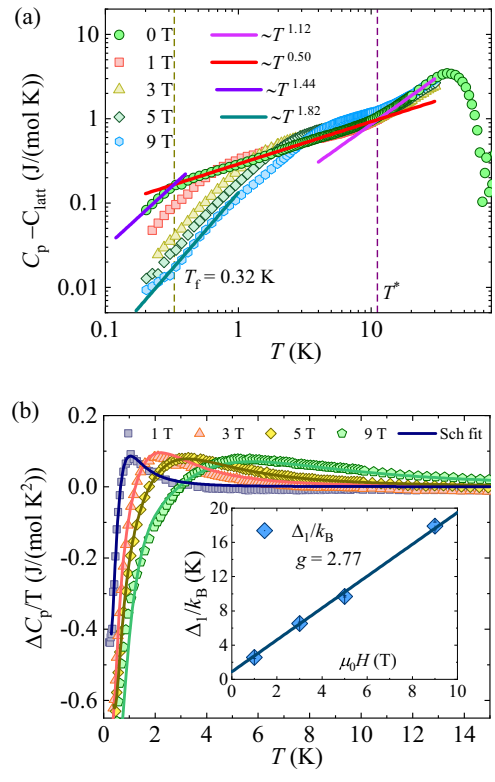

FIG. 7. (a) Temperature dependence of the residual specific heat obtained after subtracting the lattice contribution. In zero field, three distinct power-law regimes are observed, separated by two vertical lines at $T^* = 11.11$ K and $T_f = 0.32$ K. (b) Fitting of the Schottky contribution at several magnetic fields. Inset shows the estimated energy gap as a function of magnetic field.

indicating a field-induced suppression of the quasifrozen state and the emergence of an almost quadratic temperature dependence at 9 T, alluding to the field-induced emergence of exotic gapless excitations.

In order to subtract the Schottky contribution for $H \neq 0$, the zero-field data $C_p\,(0\,\mathrm{T})$ were subtracted from the corresponding data at finite fields $C_p(H \neq 0)$. The resulting $\Delta C_p/T$ data are presented in Fig. 7(b), which were fitted using the function $[C_{\mathrm{Sch}}(\Delta_1) - C_{\mathrm{Sch}}(\Delta_2)]\eta_{\mathrm{orp}}/T$, where η_{orp} represents the fraction of orphan spins, and Δ_1 and Δ_2 denote the energy gaps at finite and zero fields, respectively. The Schottky specific heat is given by $C_{\mathrm{Sch}}(\Delta) = R(\frac{\Delta}{k_{\mathrm{B}}T})^2 \frac{\exp(\frac{\Delta}{k_{\mathrm{B}}T})}{[1+\exp(\frac{\Delta}{k_{\mathrm{B}}T})]^2}$, where k_{B} is the Boltzmann constant. A similar procedure to subtract the Schottky contribution has been previously applied to materials such as Y_2CuTiO_6 [11] and $Ba_3CuSb_2O_9$ [60]. As shown in the inset of Fig. 7(b), Δ_1/k_{B} varies linearly with the applied magnetic field. The linear fit (solid line) yields a g factor of 2.77, slightly higher than the value typically observed for Cu^{2+} ($s = 1/2$) ions [11,60]. This discrepancy suggests that the orphan spins are dressed by their coupling to the surrounding RS environment. Thus the extracted gap reflects the weighted average of the local environment. At higher fields, the dominance of the high-energy tail of the gap distribution leads to an apparent g factor that exceeds the ESR value.

On the other hand, Δ_2/k_{B} increases from 0.89 to 1.7 K as the magnetic field is raised from 1 to 9 T. This gap is present already in zero field and can be attributed to spin dimers with varying gaps, which are an essential ingredient of the RS state [11,60]. After the subtraction of the Schottky contribution from the residual specific heat, the final magnetic specific heat $[C_{\mathrm{mag}}(T)]$ is presented in Fig. 3(c).

Note that the fraction of orphan spins estimated from the Schottky analysis is 3.7%, 7.01%, 8.38%, and 13% for applied magnetic fields of 1, 3, 5, and 9 T, respectively. The increasing concentration of orphan spins should not be literally interpreted as these spins are bound to the RS background. Rather, it reflects that an increasingly larger number of spins contribute to the observed Schottky behavior with increasing magnetic field.

[1] L. Balents, Spin liquids in frustrated magnets, Nature (London) **464**, 199 (2010).

[2] L. Savary and L. Balents, Quantum spin liquids: A review, Rep. Prog. Phys. **80**, 016502 (2017).

[3] S.-k. Ma, C. Dasgupta, and C.-k. Hu, Random antiferromagnetic chain, Phys. Rev. Lett. **43**, 1434 (1979).

[4] C. Dasgupta and S.-k. Ma, Low-temperature properties of the random Heisenberg antiferromagnetic chain, Phys. Rev. B **22**, 1305 (1980).

[5] F. Iglói and C. Monthus, Strong disorder RG approach of random systems, Phys. Rep. **412**, 277 (2005).

[6] H. M. Bozler, C. M. Gould, and W. G. Clark, Crossover behavior of a random-exchange Heisenberg antiferromagnetic chain at ultralow temperatures, Phys. Rev. Lett. **45**, 1303 (1980).

[7] I. Kimchi, A. Nahum, and T. Senthil, Valence bonds in random quantum magnets: Theory and application to $YbMgGaO_4$, Phys. Rev. X **8**, 031028 (2018).

[8] I. Kimchi, J. P. Sheckelton, T. M. McQueen, and P. A. Lee, Scaling and data collapse from local moments in frustrated disordered quantum spin systems, Nat. Commun. **9**, 4367 (2018).

[9] W. Hong, L. Liu, C. Liu, X. Ma, A. Koda, X. Li, J. Song, W. Yang, J. Yang, P. Cheng, H. Zhang, W. Bao, X. Ma, D. Chen, K. Sun, W. Guo, H. Luo, A. W. Sandvik, and S. Li, Extreme suppression of antiferromagnetic order and critical scaling in a two-dimensional random quantum magnet, Phys. Rev. Lett. **126**, 037201 (2021).

[10] O. Mustonen, S. Vasala, E. Sadrollahi, K. P. Schmidt, C. Baines, H. C. Walker, I. Terasaki, F. J. Litterst, E. Baggio-Saitovitch, and M. Karppinen, Spin-liquid-like state in a spin-1/2 square-lattice antiferromagnet perovskite induced by d^{10}–d^0 cation mixing, Nat. Commun. **9**, 1085 (2018).

[11] S. Kundu, A. Hossain, P. K. S., R. Das, M. Baenitz, P. J. Baker, J.-C. Orain, D. C. Joshi, R. Mathieu, P. Mahadevan, S. Pujari, S. Bhattacharjee, A. V. Mahajan, and D. D. Sarma, Signatures of a spin-$\frac{1}{2}$ cooperative paramagnet in the diluted triangular lattice of Y_2CuTiO_6, Phys. Rev. Lett. **125**, 117206 (2020).

[12] L. Liu, H. Shao, Y.-C. Lin, W. Guo, and A. W. Sandvik, Random-singlet phase in disordered two-dimensional quantum magnets, Phys. Rev. X **8**, 041040 (2018).

[13] S. Sanyal, K. Damle, J. T. Chalker, and R. Moessner, Emergent moments and random singlet physics in a Majorana spin liquid, Phys. Rev. Lett. **127**, 127201 (2021).

[14] Y. S. Choi, C. H. Lee, S. Lee, S. Yoon, W.-J. Lee, J. Park, A. Ali, Y. Singh, J.-C. Orain, G. Kim, J.-S. Rhyee, W.-T. Chen, F. Chou, and K.-Y. Choi, Exotic low-energy excitations emergent in the random Kitaev magnet Cu_2IrO_3, Phys. Rev. Lett. **122**, 167202 (2019).

[15] S. Syzranov, Effect of vacancy defects on geometrically frustrated magnets, Phys. Rev. B **106**, L140202 (2022).

[16] P. W. Anderson, Resonating valence bonds: A new kind of insulator? Mater. Res. Bull. **8**, 153 (1973).

[17] Y. Zhou, K. Kanoda, and T.-K. Ng, Quantum spin liquid states, Rev. Mod. Phys. **89**, 025003 (2017).

[18] X.-G. Wen, Quantum orders and symmetric spin liquids, Phys. Rev. B **65**, 165113 (2002).

[19] J. Khatua, B. Sana, A. Zorko, M. Gomilšek, K. Sethupathi, M. S. Ramachandra Rao, M. Baenitz, B. Schmidt, and P. Khuntia, Experimental signatures of quantum and topological states in frustrated magnetism, Phys. Rep. **1041**, 1 (2023).

[20] T. Shimokawa, S. Sabharwal, and N. Shannon, Can experimentally-accessible measures of entanglement distinguish quantum spin liquids from disorder-driven "random singlet" phases? arXiv:2505.11874.

[21] B.-J. Yang, A. Paramekanti, and Y. B. Kim, Competing quantum paramagnetic ground states of the Heisenberg antiferromagnet on the star lattice, Phys. Rev. B **81**, 134418 (2010).

[22] J. Richter, J. Schulenburg, A. Honecker, and D. Schmalfuß, Absence of magnetic order for the spin-half Heisenberg antiferromagnet on the star lattice, Phys. Rev. B **70**, 174454 (2004).

[23] Y. Qi, Z.-C. Gu, and H. Yao, Double-semion topological order from exactly solvable quantum dimer models, Phys. Rev. B **92**, 155105 (2015).

[24] H. Yao and S. A. Kivelson, Exact chiral spin liquid with non-Abelian anyons, Phys. Rev. Lett. **99**, 247203 (2007).

[25] G. Kells, D. Mehta, J. K. Slingerland, and J. Vala, Exact results for the star lattice chiral spin liquid, Phys. Rev. B **81**, 104429 (2010).

[26] S.-J. Ran, W. Li, S.-S. Gong, A. Weichselbaum, J. von Delft, and G. Su, Emergent spin-1 trimerized valence bond crystal in the spin-$\frac{1}{2}$ Heisenberg model on the star lattice, Phys. Rev. B **97**, 075146 (2018).

[27] B. H. Toby, EXPGUI, a graphical user interface for GSAS, J. Appl. Crystallogr. **34**, 210 (2001).

[28] A. Suter and B. M. Wojek, MUSRFIT: A free platform-independent framework for μSR data analysis, Phys. Procedia **30**, 69 (2012).

[29] T. Ozaki, Variationally optimized atomic orbitals for large-scale electronic structures, Phys. Rev. B **67**, 155108 (2003).

[30] H. Yoon, T. J. Kim, J.-H. Sim, and M. J. Han, Jx: An open-source software for calculating magnetic interactions based on magnetic force theory, Comput. Phys. Commun. **247**, 106927 (2020).

[31] M. Wiesmann, M. Geselle, H. Weitzel, and H. Fuess, Crystal structure of lithium copper molybdate, $Li_2Cu_2(MoO_4)_3$, Z. Kristallogr. - Cryst. Mater. **209**, 615 (1994).

[32] V. A. Efremov and V. K. Trunov, Double molybdates of alkali metals and bivalent elements, Russ. J. Inorg. Chem. **17**, 1055 (1972).

[33] J. Khatua, M. Gomilšek, J. C. Orain, A. M. Strydom, Z. Jagličić, C. V. Colin, S. Petit, A. Ozarowski, L. Mangin-Thro, K. Sethupathi, M. S. Ramachandra Rao, A. Zorko, and P. Khuntia, Signature of a randomness-driven spin-liquid state in a frustrated magnet, Commun. Phys. **5**, 99 (2022).

[34] S. S. Jahromi and R. Orús, Spin-$\frac{1}{2}$ Heisenberg antiferromagnet on the star lattice: Competing valence-bond-solid phases studied by means of tensor networks, Phys. Rev. B **98**, 155108 (2018).

[35] X. Chen, H. Liao, and Y. Li, The kagome Heisenberg antiferromagnet $YCu_3(OH)_{6.5}Br_{2.5}$: A review, J. Condens. Matter Phys. **37**, 233002 (2025).

[36] T. Arh, M. Gomilšek, P. Prelovšek, M. Pregelj, M. Klanjšek, A. Ozarowski, S. J. Clark, T. Lancaster, W. Sun, J.-X. Mi, and A. Zorko, Origin of magnetic ordering in a structurally perfect quantum kagome antiferromagnet, Phys. Rev. Lett. **125**, 027203 (2020).

[37] L. Heinze, H. O. Jeschke, I. I. Mazin, A. Metavitsiadis, M. Reehuis, R. Feyerherm, J.-U. Hoffmann, M. Bartkowiak, O. Prokhnenko, A. U. B. Wolter, X. Ding, V. S. Zapf, C. Corvalán Moya, F. Weickert, M. Jaime, K. C. Rule, D. Menzel, R. Valentí, W. Brenig, *et al.*., Magnetization process of atacamite: A case of weakly coupled $S = 1/2$ Sawtooth chains, Phys. Rev. Lett. **126**, 207201 (2021).

[38] G. Senthil Murugan, J. Khatua, S. Kim, E. Mun, K. Ramesh Babu, H.-S. Kim, C.-L. Huang, R. Kalaivanan, U. Rajesh Kumar, I. Panneer Muthuselvam, W. T. Chen, S. Krishnamoorthi, K.-Y. Choi, and R. Sankar, Spin dynamics and 1/3 magnetization plateau in the coupled distorted diamond chain compound $K_2Cu_3(MoO_4)_4$, Phys. Rev. B **111**, 144420 (2025).

[39] A. Vasiliev, O. Volkova, E. Zvereva, and M. Markina, Milestones of low-D quantum magnetism, npj Quantum Mater. **3**, 18 (2018).

[40] G. A. Bain and J. F. Berry, Diamagnetic corrections and Pascal's constants, J. Chem. Educ. **85**, 532 (2008).

[41] J. A. Quilliam, F. Bert, E. Kermarrec, C. Payen, C. Guillot-Deudon, P. Bonville, C. Baines, H. Luetkens, and P. Mendels, Singlet ground state of the quantum antiferromagnet $Ba_3CuSb_2O_9$, Phys. Rev. Lett. **109**, 117203 (2012).

[42] J. C. Fernandes, R. B. Guimarães, M. A. Continentino, H. A. Borges, J. V. Valarelli, and A. Lacerda, Titanium-III warwickites: A family of one-dimensional disordered magnetic systems, Phys. Rev. B **50**, 16754 (1994).

[43] J. Khatua, M. Gomilšek, K.-Y. Choi, and P. Khuntia, Magnetism and field-induced effects in the $S = \frac{5}{2}$ honeycomb lattice antiferromagnet FeP_3SiO_{11}, Phys. Rev. B **110**, 184402 (2024).

[44] A. Reingruber, N. Caci, S. Wessel, and J. Richter, Thermodynamics of the spin-$\frac{1}{2}$ Heisenberg antiferromagnet on the star lattice, Phys. Rev. B **109**, 125120 (2024).

[45] A. Abragam and B. Bleaney, *Electron Paramagnetic Resonance of Transition Ions* (Oxford University Press, Oxford, 2012).

[46] Z. G. Soos, K. T. McGregor, T. T. P. Cheung, and A. J. Silverstein, Antisymmetric and anisotropic exchange in ferromagnetic copper(II) layers, Phys. Rev. B **16**, 3036 (1977).

[47] C. Lee, S. Lee, H.-S. Kim, S. Kittaka, Y. Kohama, T. Sakakibara, K. H. Lee, J. van Tol, D. I. Gorbunov, S.-H. Do, S. Yoon, A. Berlie, and K.-Y. Choi, Random singlets in the $s = 5/2$ coupled frustrated cubic lattice $Lu_3Sb_3Mn_2O_{14}$, Phys. Rev. B **107**, 214404 (2023).

[48] C. Koo, J. Park, J. Werner, S. Lee, C. Balz, A. T. M. Nazmul Islam, Y. Oshima, B. Lake, K.-Y. Choi, and R. Klingeler, Two-stage evolution of magnetic correlations in the spiral spin liquid material $Ca_{10}Cr_7O_{28}$, Phys. Rev. B **111**, 125144 (2025).

[49] M. Sande, J. Khatua, Y. Choi, and K.-Y. Choi, Tuning magnetic correlations in $s = 1/2$ spin ladder $Ba_2CuTe_{1-x}W_xO_6$ through site-selective cation substitution, Phys. Rev. Mater. **8**, 094404 (2024).

[50] A. Yaouanc and P. D. De Reotier, *Muon Spin Rotation, Relaxation, and Resonance: Applications to Condensed Matter*, International Series of Monographs on Physics, Vol. 147 (Oxford University Press, Oxford, 2011).

[51] Y. J. Uemura, T. Yamazaki, D. R. Harshman, M. Senba, and E. J. Ansaldo, Muon-spin relaxation in AuFe and CuMn spin glasses, Phys. Rev. B **31**, 546 (1985).

[52] M. Gomilšek, M. Klanjšek, R. Žitko, M. Pregelj, F. Bert, P. Mendels, Y. Li, Q. M. Zhang, and A. Zorko, Field-induced instability of a gapless spin liquid with a spinon Fermi surface, Phys. Rev. Lett. **119**, 137205 (2017).

[53] J. Choi and J. V. José, Correlation effects in $S = 1/2$ random-exchange Heisenberg antiferromagnetic chains, Phys. Rev. B **35**, 419 (1987).

[54] W. Lee, S. Yoon, S. Jeon, Y. Cai, K. Kojima, G. D. Morris, B. Hitti, L. T. Nguyen, R. J. Cava, K.-Y. Choi, and S. Lee, Random singlet-like state in the dimer-based triangular antiferromagnet $Ba_6Y_2Rh_2Ti_2O_{17-\delta}$, Phys. Rev. Res. **6**, 023225 (2024).

[55] P. Popp, A. P. Ramirez, and S. Syzranov, Origin of the hidden energy scale and the f ratio in geometrically frustrated magnets, Phys. Rev. Lett. **134**, 226701 (2025).

[56] S. Pal, S. Sarkar, K. Kumar, R. Raghunathan, R. J. Choudhary, A. Banerjee, and S. B. Roy, Role of electronic excitation on the

anomalous magnetism of elemental copper, Phys. Rev. B **105**, L060406 (2022).

[57] C. Peng and L. Zhang, Scaling and data collapse of two-dimensional random singlet states in a magnetic field, Phys. Rev. B **111**, 014409 (2025).

[58] I. Živković, V. Favre, C. S. Mejia, H. O. Jeschke, A. Magrez, B. Dabholkar, V. Noculak, R. S. Freitas, M. Jeong, N. G. Hegde, L. Testa, P. Babkevich, Y. Su, P. Manuel, H. Luetkens, C. Baines, P. J. Baker, J. Wosnitza, O. Zaharko, Y. Iqbal, *et al.*, Magnetic field induced quantum spin liquid in the two coupled trillium lattices of $K_2Ni_2(SO_4)_3$, Phys. Rev. Lett. **127**, 157204 (2021).

[59] K.-Y. C. J. Khatua and G. Morris, TRIUMF μSR experiment database, https://cmms.triumf.ca/mud/runSel.html, experiment number 2392, LCMO.

[60] H. D. Zhou, E. S. Choi, G. Li, L. Balicas, C. R. Wiebe, Y. Qiu, J. R. D. Copley, and J. S. Gardner, Spin liquid state in the $S = 1/2$ triangular lattice $Ba_3CuSb_2O_9$, Phys. Rev. Lett. **106**, 147204 (2011).